Earth Planet. Sci. Lett. 668 (2025) 119540

Contents lists available at ScienceDirect

Earth and Planetary Science Letters

journal homepage: www.elsevier.com/locate/epsl

Thermodynamics of Fe-S-O-C-H liquids: Implications for the Martian core

Jac van Driel [a,*], Lidunka Vočadlo [a], John Brodholt [a,b]

[a] Department of Earth Sciences, University College London, London, WC1E 6BT, UK
[b] Centre for Planetary Habitability (PHAB), University of Oslo, N-0315 Oslo, Norway

ARTICLE INFO

Editor: J. Badro

Keywords:
Martian core
Magnetism
Iron alloys

ABSTRACT

We present a comprehensive investigation into the composition of the Martian core. We use new density functional theory (DFT) calculations, which consider in detail the magnetic properties of the Fe alloys, essential for obtaining the correct density and velocities. We then fit our results to a new Gaussian Process Regression (GPR) equation of state (EOS). Using this GPR-EOS we search for all compositions of the Martian core in the system Fe-S-O-C-H that match both the density and compressional wave speeds of a liquid Martian core throughout its entire depth range. We consider different models for the interior of Mars – in particular, those with and without a deep melt layer at the base of the Martian mantle (Irving et al., 2023; Samuel et al., 2023; Khan et al., 2023). The existence of a deep melt layer is important as it revises previous estimates for the core's size and density. We consider a range of core-mantle boundary temperatures from 1900 K to 2850 K, although we find that temperature has a relatively small effect on the possible compositions. As with previous studies, and also for the Earth, we find many different compositions that are able to match the geophysical observations of Mars' core density (ρ) and velocity (V_ϕ), regardless of which set of geophysical observations are used. All models require very high concentrations of light-elements of ≈ 50 mol% in line with previous work. The compositional variation can be reduced considerably by considering cosmochemical constraints on the maximum amount of sulphur, together with geochemical constraints on the partitioning. In this case, all solutions require very high hydrogen content of at least 0.5 wt% (27 mol%) and practically no oxygen.

1. Introduction

The recent InSight mission has significantly advanced our understanding of the Martian core, such as size, density, and seismic wave velocities. Initial analysis suggested a low-density liquid metal core with an estimated radius of 1830 ± 40 km and a density ranging from 5.7 to 6.3 g/cm^3 (Stahler et al., 2021). Subsequent refinements of the InSight seismic data adjusted this model and proposed slightly higher core densities between 6.2 and 6.3 g/cm^3 and a P-wave velocity at the top of a liquid core of between 4.9 and 5 km/s (Irving et al., 2023; Le Maistre et al., 2023; Khan et al., 2022). The evolving narrative around the characteristics of the Martian core has further been shaped by the proposal of a liquid silicate layer (LSL) at the base of the Martian mantle, as indicated by two recent studies (Samuel et al., 2023; Khan et al., 2023). These studies, leveraging differential travel times and global geophysical observations, advocate for an LSL approximately 150-170 km thick, and revise the Martian core's size down to 1,650 ± 20 km or 1,675 ± 30 km and density estimates increase to 6.5 g/cm^3 or 6.65 g/cm^3 depending on the particular study (Samuel et al., 2023; Khan et al., 2023). The presence of an LSL may bear significant consequences for the thermal properties at the core-mantle boundary, potentially elevating temperatures due to the accumulation of heat-producing elements, and indeed it has been argued that a deep melt layer may increase the temperature of the Martian CMB by up to 800 K (Samuel et al., 2021). The revised size of the core and potential increase in CMB temperature demands a reevaluation of the core's compositional models of the liquid iron core to align with observed densities and compressional wave speeds.

In this study, we combine density functional theory (DFT) and a Gaussian process regression (GPR) equation of state (EOS) to obtain the thermodynamic data for Fe-alloys across the full range of possible compositions and P-T conditions. In contrast to previous studies computational studies, (e.g. Huang et al. (2023)), we better incorporate the effect of magnetism in these alloys using a thermodynamic integration technique to obtain the correct magnetic moment for any composition and P-T condition. This is not a straightforward procedure, but we find it essential as it significantly improves the fit to experimental data. We use this to calculate the magnetic moments, densities, and internal energies of over 60 iron alloys within the Fe-S-C-O-H system from 2000 K to

* Corresponding author.
E-mail address: jack.driel.12@ucl.ac.uk (J. van Driel).

https://doi.org/10.1016/j.epsl.2025.119540
Received 15 August 2024; Received in revised form 3 July 2025; Accepted 7 July 2025

6000 K and 0 to 100 GPa. Complementing this, a GPR equation of state is fit to the DFT results. This allows us to achieve a simple but precise interpolation of a wide range of thermodynamic parameters, including seismic velocities, density, Grüneisen parameters, heat capacities, and thermal expansivities, as well as establishing rigorous confidence intervals. This GPR-based equation of state allows us to search for all possible compositions of the Martian core over different CMB temperatures and evaluate which are consistent with the geophysical models for the Martian core along self-consistent adiabatic geotherms.

Beyond geophysical data, experimental insights into elemental partitioning—particularly the interactions between sulfur, oxygen, and carbon within Fe-alloys under Martian core conditions—offer additional constraints. These findings highlight the tradeoffs when investigating the feasibility of multi-component iron alloys (Tsuno et al., 2018; Gendre et al., 2022). Indeed, when combined with cosmochemical estimates of the maximum S content on the Martian core (Steenstra and van Westrenen, 2018), such studies afford a more nuanced understanding of the core and potentially discriminate between proposed geophysical models of the Martian core.

2. Methods

The objective of this work is to obtain the range of liquid compositions that agree with the observed ρ and V_ϕ of the Martian core as inferred from InSight data (Stahler et al., 2021; Irving et al., 2023; Le Maistre et al., 2023; Khan et al., 2022). The methods can be divided into three fundamental steps.

First, density functional theory (DFT) simulations are used to calculate the pressure and internal energy of 60 distinct compositions at pressures between 0-100 GPa and temperatures from 2000-6000 K. This results in a dataset of 716 unique data points.

Second, we obtain a more accurate depiction of the magnetic state of the Fe-S-O-C-H system and thus reduce discrepancies in pressure between calculations and experiments (Huang et al., 2023; Kawaguchi et al., 2022; Kuwayama et al., 2020; Assael et al., 2006; Morard et al., 2013, 2018; Nishida et al., 2020, 2016; Shimoyama et al., 2016; Nakajima et al., 2015; Xu et al., 2021; Terasaki et al., 2019; Zhao et al., 2023; Shimoyama et al., 2013; Chen et al., 2014; Kawaguchi et al., 2017; Terasaki et al., 2010). This process involves determining the difference in Helmholtz free energy between finite magnetic states as described in Holmstrom and Stixrude (2015) and Edgington et al. (2019). Following the identification of the lowest free energy magnetic state, a simple compositional dependent pressure correction is developed which is then applied to the entire dataset of non-magnetic simulations. This correction can also be applied to other studies.

Finally, we develop a Gaussian process equation of state (GPR-EOS) to interpolate density and internal energy across pressure, temperature, and compositional space. The strength of the Gaussian process equation of state is that it can interpolate density and internal energy, and all their derivative thermodynamic properties for multi-component compositions self-consistently. It also does not require a predefined functional form for either the end-members or for the mixing. Additionally, our approach allows for the derivation of self-consistent, compositionally dependent adiabats, providing an additional constraint on the core's properties. A detailed outline of each of these steps is defined below.

2.1. Non-magnetic calculations

All calculations were performed using the Vienna Ab initio Simulation Package (VASP), a widely used package for performing ab initio molecular dynamics (AIMD) calculations (Kresse and Hafner, 1993, 1994; Kresse and Furthmuller, 1996b,a). We employed the PBE exchange-correlation function and the Fe_{pv}, S, O, C and H projector augmented wave (PAW) pseudopotentials (Blochl, 1994; Perdew et al., 1997; Kresse and Joubert, 1999), in which the pseudopotential for iron contains fourteen valence electrons.

A single k-point at the gamma point was used to sample the Brillouin zone. We set an energy cutoff of 400 eV and ensured that energies converged to within 6.4 meV/atom. All molecular dynamics calculations were conducted using the Nose-Hoover thermostat with the canonical ensemble (NVT) and a one picosecond (ps) timestep. Pulay corrections to pressure and energy were made by single-point calculations of at least ten snapshots from every simulation to a 3×3×3 k-point mesh centred on the gamma point and 1000 eV plane-wave cutoff.

Initial simulation structures start as random amorphous structures generated using *ab-initio* random structure searching (AIRSS), with the first two ps of the simulation designated for equilibration (Pickard and Needs, 2011). Depending on composition, pressure, and temperature, the subsequent time steps, ranging from 8-15 ps are used for analysis. The uncertainty in pressure, temperature and internal energy of a simulation were obtained using the blocking method, which accounts for autocorrelation within the simulation (Flyvbjerg and Petersen, 1989).

2.2. Magnetic calculations

Accurately accounting for magnetism when studying iron alloys at low pressures is crucial (Holmstrom and Stixrude, 2015; Edgington et al., 2019). Specifically, iron atoms within liquid iron alloys typically exhibit elevated spin states at pressures below 50 GPa, which can significantly alter the volume of a system under a given P-T condition (Edgington et al., 2019). Unfortunately, VASP and other DFT codes do not routinely include the entropy of magnetic moment within the inner energy minimisation loop, and so this has to be corrected afterwards. The correct magnetic moment of a given atom can be determined by thermodynamic integration (Holmstrom and Stixrude, 2015; Edgington et al., 2019). This method establishes the difference in Helmholtz free energy between various magnetic states, incorporating the entropic contribution.

For a specific composition, the difference in free energy between a magnetic state, $F_{\mu_B}(V,T)$, and the corresponding non-magnetic reference state, $F_0(V,T)$, is defined as

$$F_{\mu_B}(V,T) - F_0(V,T) = \Delta F(V,T) - T S_{\mathrm{mag}}(V,T,n), \tag{1}$$

where $\Delta F(V,T)$ is the free-energy change (excluding magnetic entropy) when switching from non-magnetic to magnetic configurations, and $S_{\mathrm{mag}}(V,T,n)$ is the magnetic contribution to the entropy:

$$S_{\mathrm{mag}}(V,T,n) = k_B \sum_{i=1}^{n} \ln\left(|\mu_i| + 1\right). \tag{2}$$

Here μ_i is the spin state of the i^{th} atom, n is the number of Fe atoms, and k_B is the Boltzmann constant. The free-energy difference $\Delta F(V,T)$ is obtained via thermodynamic integration:

$$\Delta F(V,T) = \int_0^1 \langle U_{\mu_B}(\lambda) - U_0(\lambda) \rangle_\lambda \, d\lambda. \tag{3}$$

In practice, for each composition, we compute the potential energy difference between the non-magnetic and magnetic systems at three different values for λ, (0,0.5,1).

Once $\Delta F(V,T)$ is obtained, we fit the Helmholtz free-energy difference for that specific composition, volume, and temperature to

$$F_{\mu_B} - F_0 = A \exp\left(B\langle\mu_B\rangle\right) - C\langle\mu_B\rangle - D, \tag{4}$$

where A, B, C, and D are constants for each composition. These parameters do not carry a direct physical meaning, but minimising this expression allows us to obtain the correct moment $\langle\mu_B\rangle$ for that composition, V and T. All fits for each composition are provided in the supplementary information, along with the 2σ uncertainty in $\langle\mu_B\rangle$. This uncertainty is propagated to the pressure by evaluating the pressure at the upper and lower bounds of $\langle\mu_B\rangle$. Typical corrections to the pressures are not large and are of the order of a few GPa, but are particularly

Table 1
Magnetic Corrections.

Parameter	Value	Units
A	14.48	GPa
B	11.10	g/cm^3
C	0.50	cm^3/g
D_S	-10.00	g/cm^3
D_O	-0.10	g/cm^3
D_H	-0.10	g/cm^3
D_C	-8.94	g/cm^3
E	0.12	[unitless]

important for fitting to the low pressure data. Unfortunately, the uncertainty on the pressure correction can be quite large because the local minimum in F_{μ_B} is relatively flat (see supplementary information).

After the magnetic state is refined for a subset of compositions and P-T conditions, we perform new fixed-spin calculations to capture the effect of the correct magnetism. To extend these results to all other compositions and conditions—without incurring prohibitive computational costs—we construct a compositionally dependent pressure correction, P_C, based on the functional form as suggested by Li et al. (2022), to fit difference in pressure between the zero-moment and refined-moment systems:

$$P_{\mathrm{C}} = A \cdot \mathrm{X}_{Fe} \cdot \mathrm{F} \cdot \frac{1}{1 + \exp\left[(\rho - \rho_{\mathrm{eff}}) \cdot C\right]} \tag{5}$$

where:

$$\rho_{\mathrm{eff}} = B + D_S \cdot \mathrm{X}_S + D_O \cdot \mathrm{X}_O + D_H \cdot \mathrm{X}_H + D_C \cdot \mathrm{X}_C \tag{6}$$

and

$$\mathrm{F} = 1 + E \cdot (\mathrm{X}_S + \mathrm{X}_O + \mathrm{X}_H + \mathrm{X}_C). \tag{7}$$

Were, ρ is the density in g/cm^3, and $\mathrm{X}_{Fe,S,O,H,C}$ are the mole fractions. The interaction factor F scales the correction based on the total non-Fe content. The parameters for the magnetic corrections are in Table 1. The pressure correction is then applied to all the other simulations run without magnetism.

Following Li et al. (2022), a correction is also added to the internal energy, U_C

$$\Delta U_C = -\int_{V_0}^{V_C} \Delta P_C dV \tag{8}$$

where V_0 is the volume of uncorrected calculation at pressure P_0, and V_C is the volume at the corrected pressure, P_C. V_C are obtained from the GPR-EOS fit. The entire corrected dataset can be found in Table 1 of the supplementary information.

2.3. Gaussian process equation of state

The final step in our methodology involves using a Gaussian process equation of state to interpolate pressure and internal energy across density, temperature, and compositional space (Rasmussen and Williams, 2006; Gardner et al., 2018a,b). Two separate multidimensional surfaces for pressure Φ and internal energy Ψ, were formulated as a function of composition (Fe, S, O, H, C), the density (ρ), and the temperature (T), such that pressure, P, and internal energy, U, can be expressed as:

$$P = \Phi(Fe, S, O, H, C, \rho, T) \tag{9}$$

$$U = \Psi(Fe, S, O, H, C, \rho, T) \tag{10}$$

Partial derivatives are then obtained using automatic differentiation to compute the other thermodynamic properties. For example, the rate of change of pressure with respect to density is represented as $\frac{\partial \Phi}{\partial \rho}$, and similar expressions hold for the other variables. Thus, we can define the following thermodynamic relations below. The thermal expansion coefficient, α is defined as:

$$\alpha = -\frac{1}{K_T}\left(\frac{\partial \Phi}{\partial T}\right)_\rho \tag{11}$$

where,

$$K_T = \rho\left(\frac{\partial \Phi}{\partial \rho}\right)_T \tag{12}$$

The heat capacity at constant volume, C_V, represents the heat required to induce a unit temperature change in the material and is derived from the internal energy-temperature relationship:

$$C_V = \frac{1}{M}\left(\frac{\partial \Psi}{\partial T}\right)_\rho \tag{13}$$

The Gruneisen parameter γ is a dimensionless quantity that offers a relationship between a material's volume, thermal expansion, and heat capacity. It is given by:

$$\gamma = \left(\frac{\partial \Phi}{\partial T}\right)_\rho \left(\frac{\partial T}{\partial \Psi}\right)_\rho \left(\frac{M}{\rho}\right) \tag{14}$$

The isentropic bulk modulus K_S measures the compressibility of a material under adiabatic (or isentropic) conditions. It is expressed as:

$$K_S = K_T(1 + \alpha\gamma T) \tag{15}$$

Lastly, the bulk sound velocity V_Φ is a crucial parameter in seismology and material science, indicating the speed at which pressure waves propagate through a medium. It is derived from the bulk modulus and density as:

$$V_\Phi = \sqrt{\frac{K_S}{\rho}} \tag{16}$$

A critical component of our methodology is validating the accuracy of the GPR model with datasets not encountered used in training the GPR-EOS. We do this in two ways: first, we exclude the results of a number of randomly selected simulations from the whole database, encompassing a wide range of pressures and temperatures; second, the removal of a specific composition from the training dataset. Such a strategy tests how well the model works for conditions not used in training. The results of these tests are shown in Fig. 1.

The left hand side of Fig. 1 compares the expected pressure or internal energy with the GPR-EOS predictions. These are shown for the training data, validation set, and for an unseen composition of $Fe_{76.6}S_{15.6}O_{7.8}$. Most results fall very close to the 1:1 line for a perfect prediction. The right side of Fig. 1 shows the predicted properties with their uncertainties for the unseen composition not included in the training set. In this particular case, the 2-sigma uncertainties are quite large, which is due to the fact that this composition is far from those used in the training set. Other unseen compositions nearer to those used in the training set will have significantly smaller uncertainties.

Some simulations in our dataset are at conditions and compositions where thermodynamic equilibrium may result in additional phases or phase separation (e.g., diamond precipitation, Fe_3C formation, or liquid immiscibility in Fe–O–S–H systems). In practice, our ab initio molecular dynamics simulations are relatively short and with finite cell sizes, and so phase separation or solidification is unlikely to have occurred. Nevertheless, we have checked the simulations for this (RMS, radial distribution functions and visually) and exclude any suspect simulations. Nevertheless, some simulations will represent metastable single-phase states rather than true equilibrium states, but we have included these data to ensure the broadest coverage of composition, pressure, and temperature space for the Gaussian Process Regression (GPR). As well as providing data for the metastable phases, this also adds to the accuracy of the GPR-EOS and reduces uncertainty for the stable liquid phase near to phase boundaries.

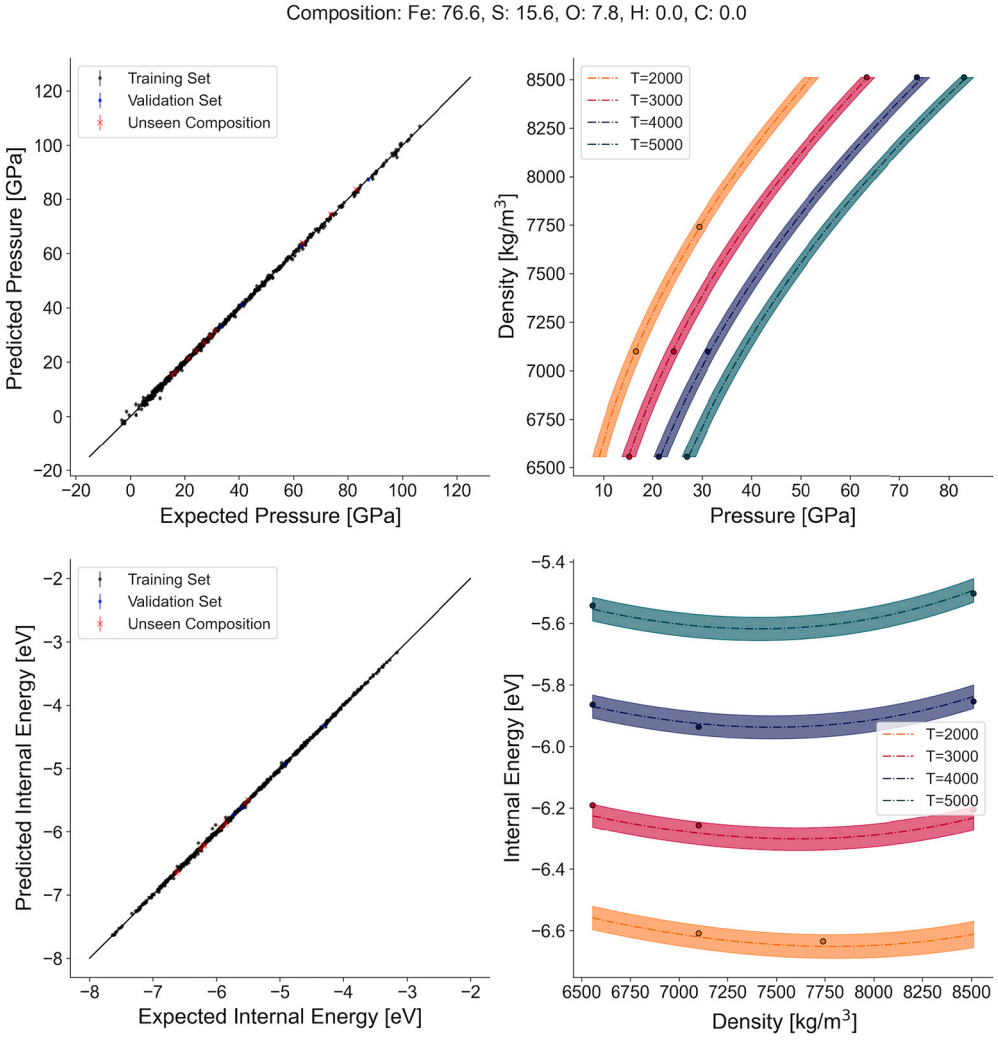

Fig. 1. GPR-EOS fitting quality for density and internal energy. The left hand side shows the expected and predicted pressure or internal energy for the training set and validation set (top and bottom respectively), and the right hand side shows the fit to an entirely unseen composition ($Fe_{76.6}S_{15.6}O_{7.8}$). The validation set is randomly sampled across pressure, temperature, and composition, while the unseen composition is not included in the training set. Fits are shown with their 2-sigma confidence interval.

3. Results

The role of magnetism in the properties of materials, especially in low-pressure iron alloys, is significant (Holmstrom and Stixrude, 2015; Edgington et al., 2019). Given the relatively low pressure and temperature range for small planets, we pay close attention to magnetism and its associated effects as discussed in the Methods section. The magnetic moment and its effect on pressure from thermodynamic integration are shown in Fig. 2 for a wide range of compositions and temperatures. Our results agree with those presented by Edgington et al. (2019), which demonstrated that the magnetic moment of iron atoms within iron alloys decreases approximately logarithmically from ~2 Bohr Magnetons per atom under ambient conditions to around ~1 Bohr Magneton per atom at approximately 100 GPa (Waseda and Suzuki, 1970; Weber et al., 1978; Edgington et al., 2019). Our results also show that iron atoms in liquid FeO have the highest magnetic moments of an individual iron atom, surpassing those in FeS, FeC, FeH, and even pure iron. Additionally, the results show a direct correlation between elevated temperatures and an increased magnetic moment, consistent with the influence of magnetic entropy.

The effect of the correct magnetic moment on pressure is also shown in Fig. 2 and highlights the need for a different correction for different compositions and not a simple constant correction as applied in other studies (Huang et al., 2023). Although FeO has the highest magnetic moment per iron atom, it still contains half the total number of iron atoms compared to pure iron, and so the effect of the correct magnetic moment on pressure is lower than pure iron. Explicitly pure iron requires a magnetic correction of ~12.5 GPa at ambient conditions, decreasing to ~8 GPa at 100 GPa. On the other hand, FeO requires a pressure correction of about 8 GPa at ambient conditions, also decreasing with pressure. The effect of magnetism on pressure for the other compositions are also shown. We have also plotted the fit of the parametrised equation for the magnetic pressure correction (Eqn. (5)) for different compositions. This compositionally dependent treatment of magnetism and its associated pressure difference is important as it improves the fit between computational and experimental results (shown in Fig. 3).

Fig. 3 compares our GPR-EOS predictions for density and compressional wave speed (V_ϕ) with various experimental datasets. In all cases, the experimental data plotted differ by no more than ±600 K from the isotherm and by no more than ±2 mol% from the composition used in our GPR-EOS calculations. This grouping ensures that multiple published data points can be collectively compared with our models on a single curve, even if the exact composition or temperature reported in the experiments is slightly shifted from our nominal isotherm. A table of our predictions to the experimental data in the Supplementary Information is provided for an exact comparison.

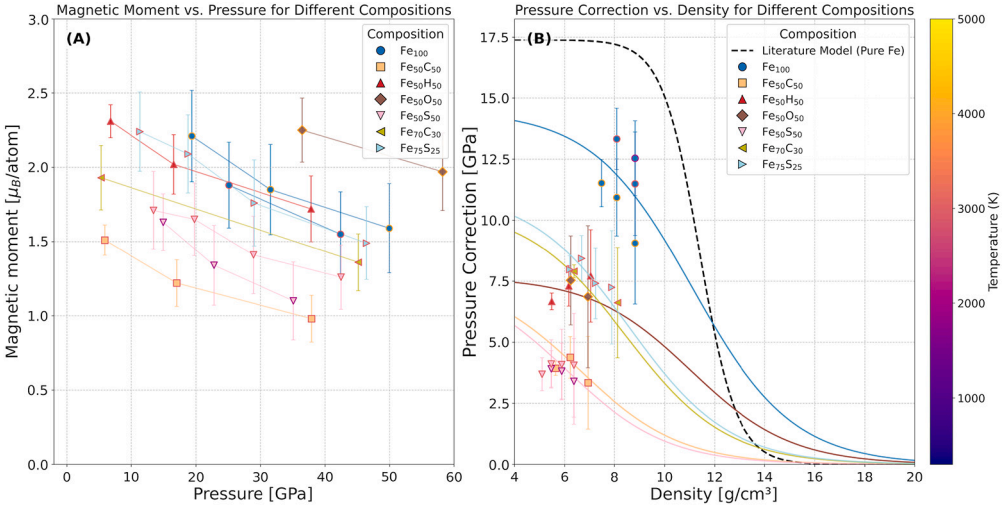

Fig. 2. (A) Magnetic moments from thermodynamic integration as a function of pressure for various compositions. Data points with the same composition and temperature are connected by lines. The magnetic moments display a similar trend to that reported by Edgington et al. (2019), with values decreasing from approximately 2.3 μ_B/atom at ambient conditions to around 1.5 μ_B/atom at 50 GPa. The iron atoms in $Fe_{50}O_{50}$ exhibit the highest magnetic moments across the pressure range, while $Fe_{50}C_{50}$ consistently has the lowest values. (B) Pressure correction (difference between magnetic and non-magnetic pressure) as a function of density for the same compositions. Coloured lines represent the empirical pressure correction model (Eqn. (5)), while the dashed black line shows the literature model for pure iron from Li et al. (2022). Pure iron (Fe_{100}) demonstrates the most significant pressure correction, reaching ~13.5 GPa at low densities. All compositions show a systematic reduction in pressure correction with increasing density, following a sigmoidal pattern that approaches zero at high densities. The pressure correction is relatively temperature-insensitive within the measurement uncertainties shown by the error bars.

In general there is a good fit for both pure iron and various Fe-S and Fe-C alloys with most experiments falling within error of our predictions. Although not all experimental data agree with our results, this is not surprising as there are inconsistencies between and even within experimental data sets. For instance, the densities of Chen et al. (2014) for FeS up to about 5 GPa are considerably higher than ours, but on the other hand, these do not agree with the more recent experiments of Morard et al. (2018). For pure Fe, our predictions are in excellent agreement with experiments at 3200 K and higher pressure by Kuwayama et al. (2020).

The higher pressure experiments of Morard et al. (2013) at around 2000 K for the 20 mol% S systems are somewhat lower than we predict. However, we argue that they are not consistent with the measured p-wave velocities for the Fe-S system. This is shown in Fig. 3B, where we fit their volumes to obtain a bulk modulus, which together with an adiabatic correction to the bulk modulus, provides the wave speed. As can be seen this is much higher than the experimentally measured velocities on similar systems.

At higher temperatures of around 3400 K the $Fe_{75}S_{25}$ densities of Kawaguchi et al. (2022) are a little lower than ours, as are those of Morard et al. (2013). However, the two datasets seem to show approximately the same density despite quite different temperatures and compositions.

Our predicted densities for the Fe-C and the Fe-C-S system are in excellent agreement with all available experiments.

For compressional wave speed, our model demonstrates good agreement with experiments for both Fe-C and Fe-S systems, especially at higher pressures appropriate for the Martian core. At lower pressures we also have good agreement with the experiments for pure iron and the Fe-S end-member of Nishida et al. (2020), albeit with some discrepancies for intermediate Fe-S compositions at lower pressures. However, it is important to note that as pressure increases the velocities for all compositions tend towards each other. For instance, at 20 GPa and 2000 K, both our model and the experiments predict a compressional wave speed of 5 km/s for pure iron compared to 4.8 km/s for FeS.

Overall, our equation of state provides a good fit to much of the data, especially when considering that experimental studies on similar systems are not always in good agreement with each other, even at low pressure. Also, obtaining densities of melts in high-pressure experiments is extremely challenging and involves many steps.

Our study differs significantly from the recent study of Huang et al. (2023) which also used ab initio simulations to obtain the thermodynamic properties of the Fe-alloys. In particular, we predict a smaller effect of light elements on densities, and so we need a greater concentration of light elements within the Martian core than Huang et al.'s model would predict (see results below). The difference in velocities is also large and varies strongly depending on the particular composition. For instance, Huang et al. (2023) predict a greater dependence of velocity on S composition, with a predicted V_ϕ of just 4.2 km/s for $Fe_{78}S_{22}$; this low value is however, far lower than the values of 4.8 km/s found experimentally and predicted by us. A comparison between our results and Huang et al. (2023) is shown Figure 7 and 8 in the SI.

Despite nominally using the same methods (DFT simulations), there are two main differences between the results of our study and those of Huang et al. (2023). First is the treatment of the pressure correction due to magnetism, in which the pressure correction used in our research is derived from minimising the magnetic free energy of the system (see above). As such the correction is less important at higher pressures as magnetism decreases and also depends on composition. In contrast Huang et al. (2023) used a simple density-dependent correction with no dependence on composition. Second, is the treatment of the internal energy correction. Unlike the study by Huang et al. (2023), we add a correction to the internal energy, which is defined by the integral of pressure and volume (Eq (8)). This correction of the internal energy and the correct handling of magnetism is crucial to obtain the correct thermodynamic properties of the system, in particular density and compressional wave speed, and ultimately the inferred composition of the Martian core.

Fig. 4 shows an example of our predicted thermodynamic properties. In this particular case, we highlight binary FeX compositions with a concentration of 25 mol% light element. They are all plotted along their own self-consistent adiabat starting at 2000 K. As expected, the density of Fe is much higher than that of the alloys, and above 25 GPa the greatest effect on density goes from S to O and then to C and H. This order is in agreement with that found by Badro et al. (2014) for the Earth's core. However, the behaviour of V_ϕ is very different under Mar-

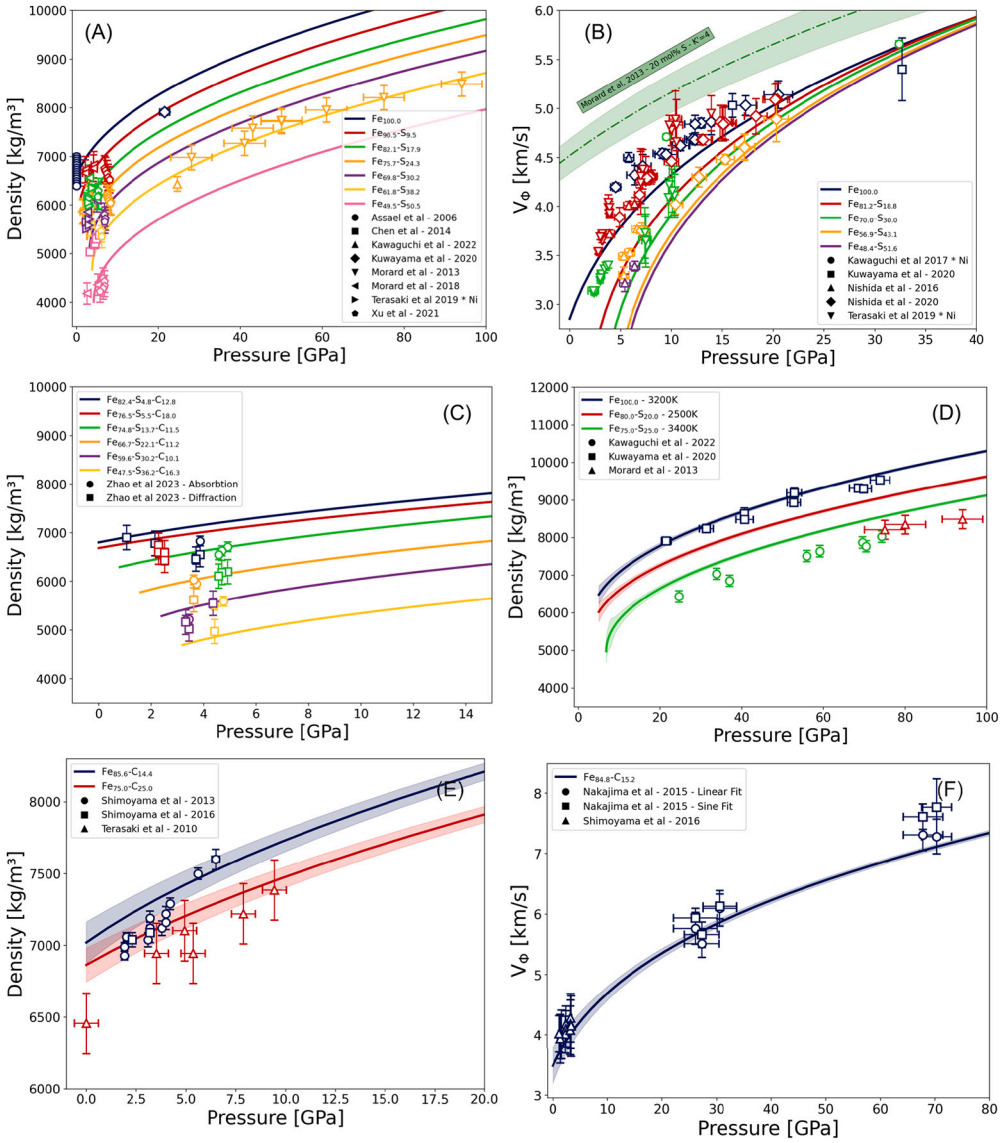

Fig. 3. A comparison of our thermodynamic model for density and compressional wave speed with various experimental studies. (A) displays the density of the FeS system along a 2200 K isotherm. (B) displays V_ϕ of FeS system along a 2100 K isotherm. (C) displays density of FeSC system along a 1800 K isotherm. (D) displays density of the FeS system along a 3000 K isotherm. (E) displays density of FeC system along a 1800 K isotherm. (F) displays V_ϕ of the FeC system along a 2200 K isotherm. The experimental data shown lies within ± 600 K and ± 2 mol% from the modelled isotherms to accommodate the slight differences of temperatures and compositions in the experiments. See text for more discussion.

tian conditions than the Earth's. Under Earth's core-conditions all light elements increase V_ϕ (Badro et al., 2014; Umemoto and Hirose, 2020) as the effect of the light element on density outweighs their effect on the bulk modulus. But under the lower P&T conditions of Mars, Fe-S and Fe-O both have lower velocities than pure Fe, with Fe-C and Fe-H having higher velocities. Above ≈50 GPa the velocity of all alloys starts to become higher than pure Fe as happens in the Earth. As we show later, carbon may be an important light element in the Martian core as it reduces the density of FeX alloys, while simultaneously offsetting the effect the other light elements have on reducing the compressional wave speed.

Fig. 5 illustrates the comparative effects that light element concentration and temperature of the CMB have on density and V_ϕ. To do this, we have chosen an arbitrary composition, although any other composition could have been used for this example. These are plotted along an appropriate compositionally dependent adiabatic geotherm, but starting at different CMB temperatures. As can be seen, a difference of 800 K in the CMB temperature (which encompasses the largest variation suggested in the literature) changes the density by about 5%. This is similar to that produced by a change in total light element concentration of only about 3 mol%, a relatively modest amount considering Mars' core should have about 50 mol% light element concentration. Large variations in CMB temperature have an even smaller effect on V_ϕ of only 1%. In other words, any inversions for the composition of Mars' core will be relatively insensitive to the chosen CMB temperature.

It is also worth noting that not only is seismic velocity insensitive to CMB temperature, it appears to be relatively insensitive to Mars' core composition in comparison with density. For instance, an 8% increase in light element decreases density by about 8%, but V_ϕ changes by only 2%. Nevertheless, as shown below, density and V_ϕ have to be fit together to constrain core composition.

It is worth mentioning that we have omitted nickel in our compositions. However, compared to the light elements, the effect of nickel on density is minimal; for example, Huang et al. showed that the density decreases from 8083 kg/m^3 to 8057 kg/m^3 between pure Fe and $Fe_{85}Ni_{15}$ at 19 GPa and 2100 K, and the density decreases from 8640

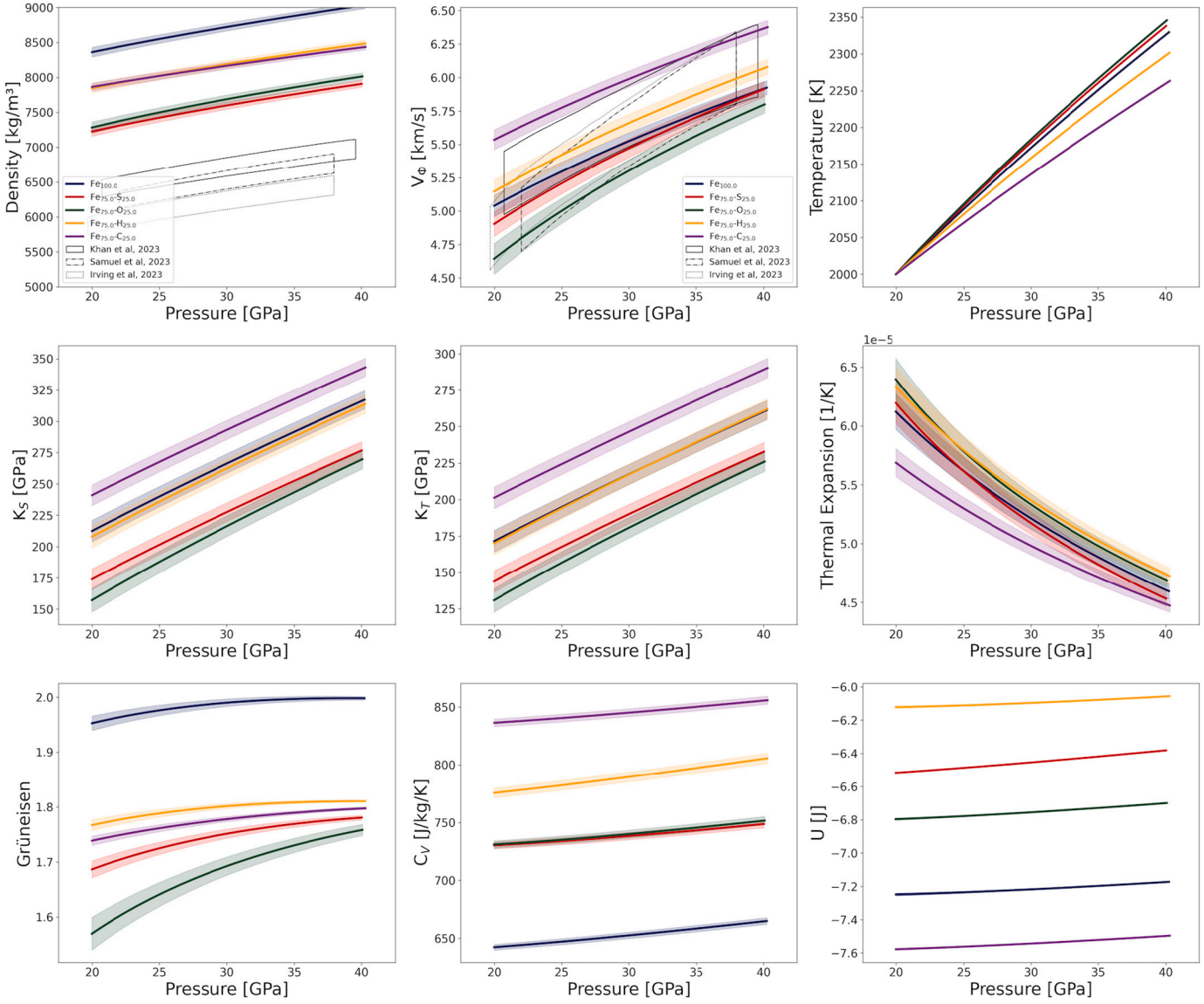

Fig. 4. Thermodynamic properties of liquid iron (Fe_{100}) and the binary alloys at 25 mol% light element, all computed along a self-consistent adiabat starting at 2000 K. Shaded bands are 2σ uncertainties. The top row displays density and compressional wave velocity (V_ϕ) as functions of pressure, as well as the corresponding thermal profiles along the self-consistent adiabats. Dashed black lines are three published geophysical models for the Martian core (Irving et al., 2023; Samuel et al., 2023; Khan et al., 2023) for comparison between our binary-alloy results and inversion-based compositions. The middle row shows the isentropic and isothermal bulk moduli, K_S K_T. The bottom row is the thermal expansion coefficient α, Grüneisen parameter γ, and heat capacity at constant volume (C_V). Notably, Fe–C and Fe–H have higher (V_ϕ) than pure Fe under these conditions, whereas other light elements reduce (V_ϕ). This contrasts with Earth's core conditions, where all light elements tend to increase compressional velocity.

kg/m^3 to 8639 kg/m^3 between pure Fe and $Fe_{85}Ni_{15}$ at 35 GPa and 2400 K (Huang et al., 2023). As such we assume moderate amounts of Ni will not change our conclusions.

4. Martian core composition

Fig. 6, shows our predicted velocities and densities for suggested core compositions from recent studies (Irving et al., 2023; Samuel et al., 2023; Khan et al., 2023). Our model suggests the compositions of Irving et al. (2023); Samuel et al. (2023) somewhat overestimates density relative to their seismic inversions for Vp and density, and would therefore require a greater concentration of light elements. Despite these discrepancies in density, both of these compositions successfully match the observed seismic velocity V_ϕ. Conversely, the composition suggested by Khan et al. (2023) fails to both match their density and V_ϕ inversion. An additional composition from Khan et al. (2023) was not plotted because its high light-element concentration, namely $Fe_{35.2}S_6O_{6.4}H_{18.6}C_{33.8}$, which places it outside the training data; however, based on its composition, it would likely significantly underestimate density. This failure to match the compressional wave speed can be attributed to the underlying thermodynamic model of Huang et al. (2023) used by Khan et al. (2023). As discussed earlier, the thermodynamic model of Huang et al. (2023) only made a simple constant correction for magnetism and did not incorporate an internal energy corrections to the individual calculations. It is not surprising then that we predict different compositions for the Martian core.

Using our GPR-based equation of state, we now search for possible Martian core compositions that do fit the seismic data. We first start by examining binary and ternary compositions as these are convenient to display graphically. A successful composition is one where the predicted density and V_ϕ along a self consistent adiabat agrees within error (2σ) with the seismic model across the whole pressure range of the core.

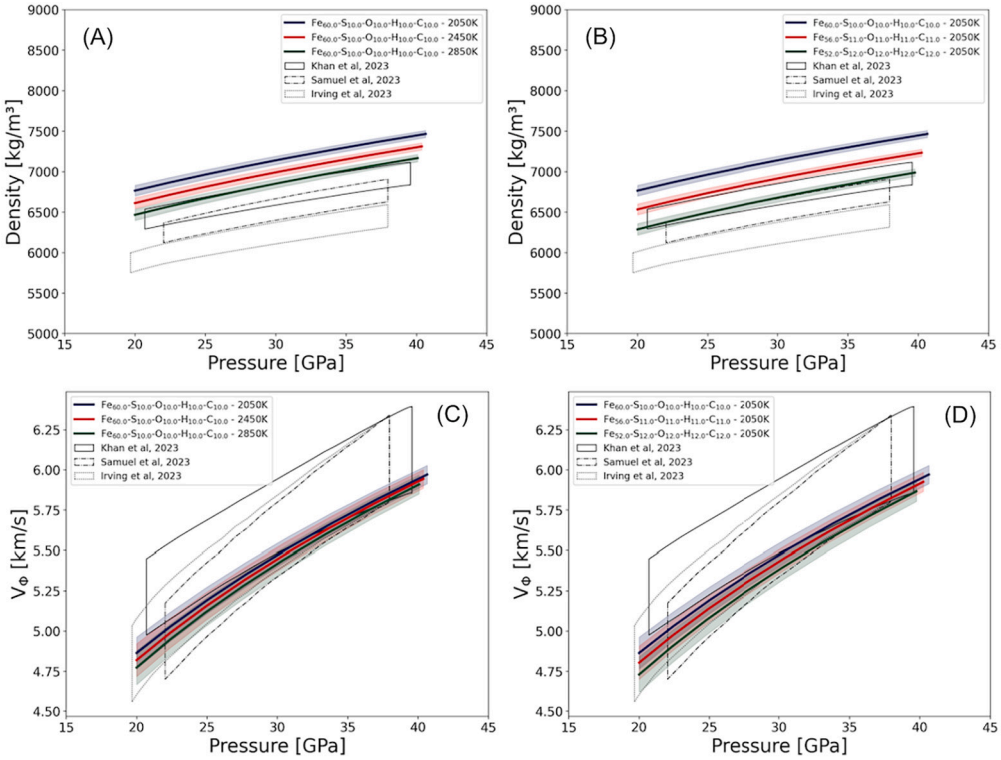

Fig. 5. A comparison of the effect of varying CMB temperatures and light element concentration on both density and V_ϕ. The compositions are completely arbitrary and we could have used any other composition for this comparison. All profiles are calculated along a self-consistent adiabat. The boxes represent the range in density and velocity for Mars' core from three recent studies and are shown as guide to the variation between different studies. In the case of Samuel et al. (2023), we take their inversion but use a 2-sigma uncertainty taken from Khan et al. (2023) See text for a discussion.

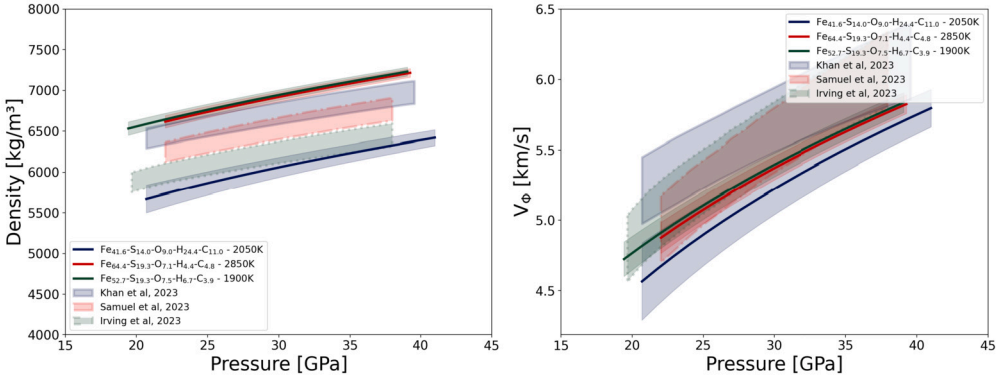

Fig. 6. Green, red and blue lines and their confidence limits are the density and V_ϕ for the three core compositions of Irving et al. (2023), Samuel et al. (2023) and Khan et al. (2023) respectively as predicted by our GPR-EOS. The temperatures are along the self-consistent adiabat using the proposed CMB temperatures from the three studies. Also shown are the proposed density and velocity profiles for the Martian core inverted from the geophysical observations from the same three studies. According to our work, none of these compositions are able to fit any of the proposed density and velocity profiles.

For each seismic model at least 2,000 compositions are tested. Detailed results can be found in the supplementary information.

4.1. No melt-layer model

First we concentrate on the model of Irving et al. (2023), which does not include a deep mantle liquid silicate layer and proposes a somewhat larger and lower-density Martian core of about 1830 km radius, a CMB temperature of 1900 K, a density of about 6.2 to 6.3 g/cm^3 and a V_ϕ of about 4.9 to 5 km/s at the top of the core. The results for ternary systems are shown in Fig. 7.

If we start by considering density alone, then S, O and C are all able to match the density of the Martian core given by Irving et al. (2023). However, the concentrations are very high and depending on the particular light element, can range from 50 mol% for S to over 60 mol% in the case of C. Of course, as also shown, there are then many ternary compositions which will work, as well as higher order concentrations discussed later.

The compositional space is reduced somewhat by including V_ϕ in the fit (as shown by the green dots in Fig. 7), and we find that none of the light elements are able to match the geophysical constraints alone. Moreover, all pairs of light elements (i.e. ternary compositions) require the inclusion of C to match both density and V_ϕ. Most matching ternary compositions, either Fe-S-C or Fe-O-C, however, show roughly horizontal bands across the ternaries. This means that the total concentration of light elements is approximately similar in all cases, and total concentrations of light elements of between 45 mol% to 60 mol% are required.

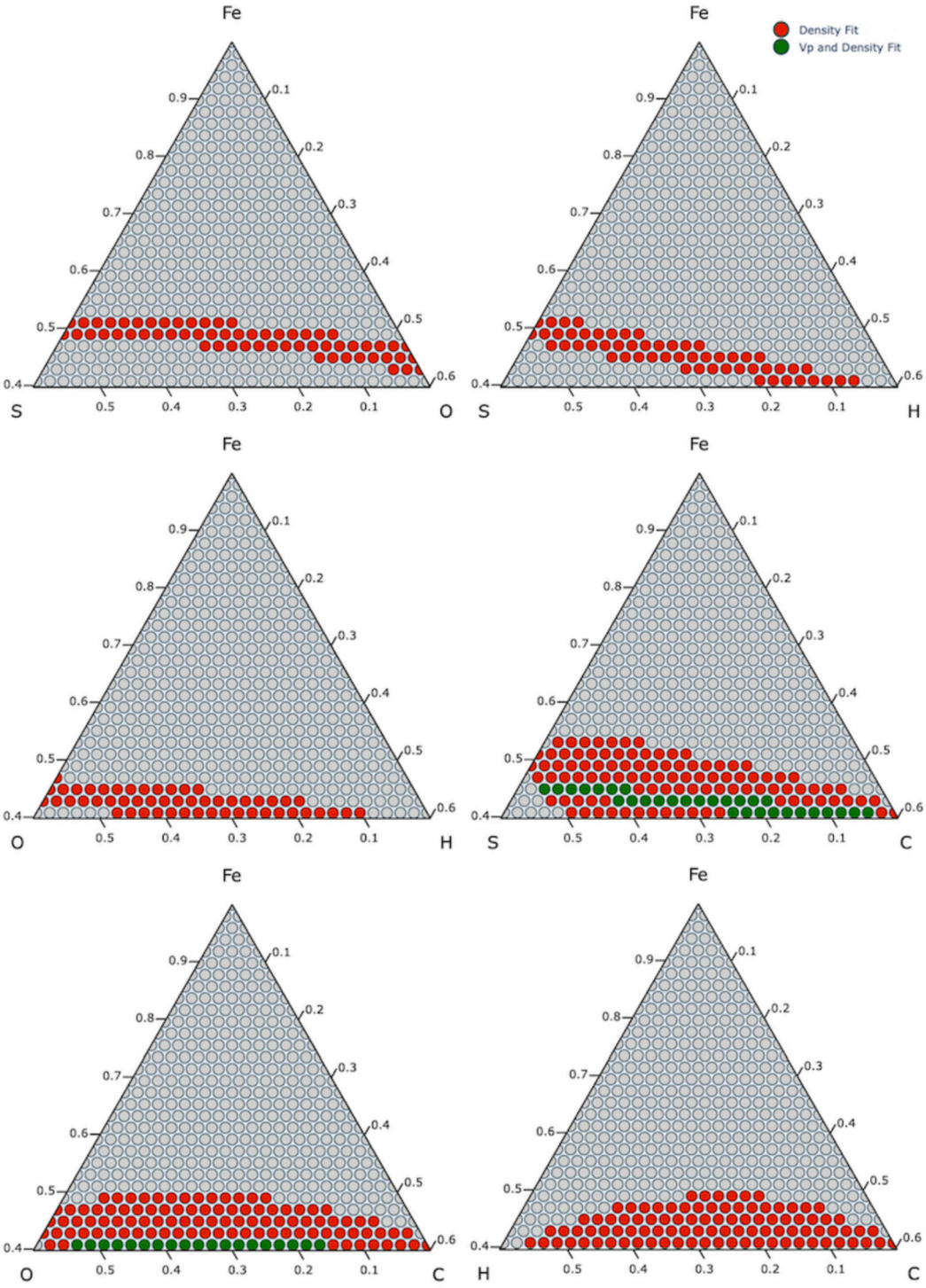

Fig. 7. Ternary plots showing compositions which match either the density (red) or both the density and V_ϕ (green) for the model of Irving et al. (2023). We define a successful match as when the 2-sigma confidence limits of the GPR prediction overlaps the 2-sigma confidence limits in the geophysical model at all core depths. We assume that the geophysical confidence limits are similar to those in Khan et al. (2023). The inversion assumes a starting temperature of the Martian CMB of 1900 K as suggested by the work of Irving et al. (2023).

These concentrations of light element are higher than those suggested from cosmochemical and other constraints, (e.g. Steenstra and van Westrenen (2018); Brennan et al. (2020); Khan et al. (2022); Gendre et al. (2022)). For instance, Steenstra and van Westrenen (2018) limits the maximum amount of S to about 17 wt% (about 26 mol%) and so S cannot be the sole light element and has to be combined with equally large concentrations of O, C or H to match density. Applying these additional constraints is addressed below.

4.2. Melt-layer model

There are two similar models for the Martian interior which find evidence for a deep mantle layer just above the core, and both inversions result in a smaller and denser core (Samuel et al., 2023; Khan et al., 2023). As such, the concentration of light elements is reduced in both models (Figs. 8 and 9). The primary difference between the two models is that Samuel et al. (2023) suggest that the melt layer should produce a

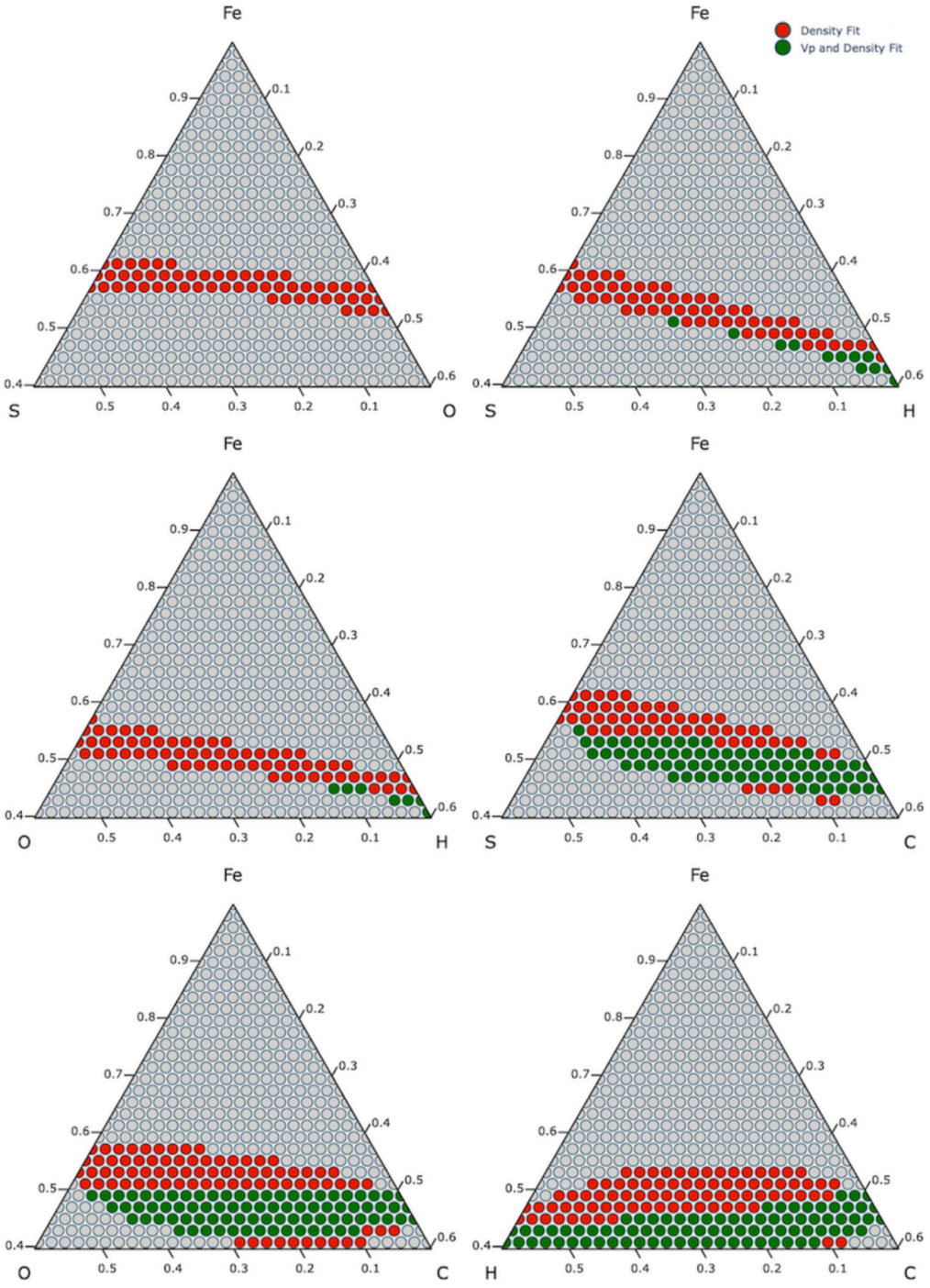

Fig. 8. This figure is similar to Fig. 7 but this time shows chemical compositions for the Martian core which fit the geophysical model of Khan et al. (2023). Red points are where just density is matched, while green points are where both density and V_ϕ are matched within 2 sigma of both the geophysical inversions and our GPR equation of state. The inversion assumes a starting temperature of the Martian CMB of 2050 K as suggest by the work of Khan et al. (2023).

much hotter core, 2850 K rather than 2050 K from Khan. Additionally, the model of Samuel et al. (2023) has a higher density liquid silicate layer and thus a somewhat lower density core. Nevertheless, differences in temperature and density of the core negate each other, resulting in fairly similar patterns of light element concentrations that fit both the models of Samuel et al. (2023) and Khan et al. (2023).

As with compositions which fit the model of Irving et al. (2023), using V_ϕ as well as density significantly reduces the compositional space. And again, appropriate binaries generally produce sub-horizontal bands across the ternaries, indicating that the light element composition is approximately constant in terms of mol%, and the particular element plays a secondary role. These differences are of course greatly amplified when considering wt% due to their different molar masses, especially H.

For both of the models with a melt layer we find that two purely binary mixtures can match both V_ϕ and density. These are Fe-H and Fe-C, at molar concentrations of 60 and 55 mole% respectively. We also find solutions within all ternaries, with the exclusion of Fe-S-O.

Of course, as with the models of Irving et al. (2023), many of the compositions which match the models of Khan et al. (2023) and Samuel et al. (2023) would be excluded by considering partitioning and cosmochemical constraints (see below).

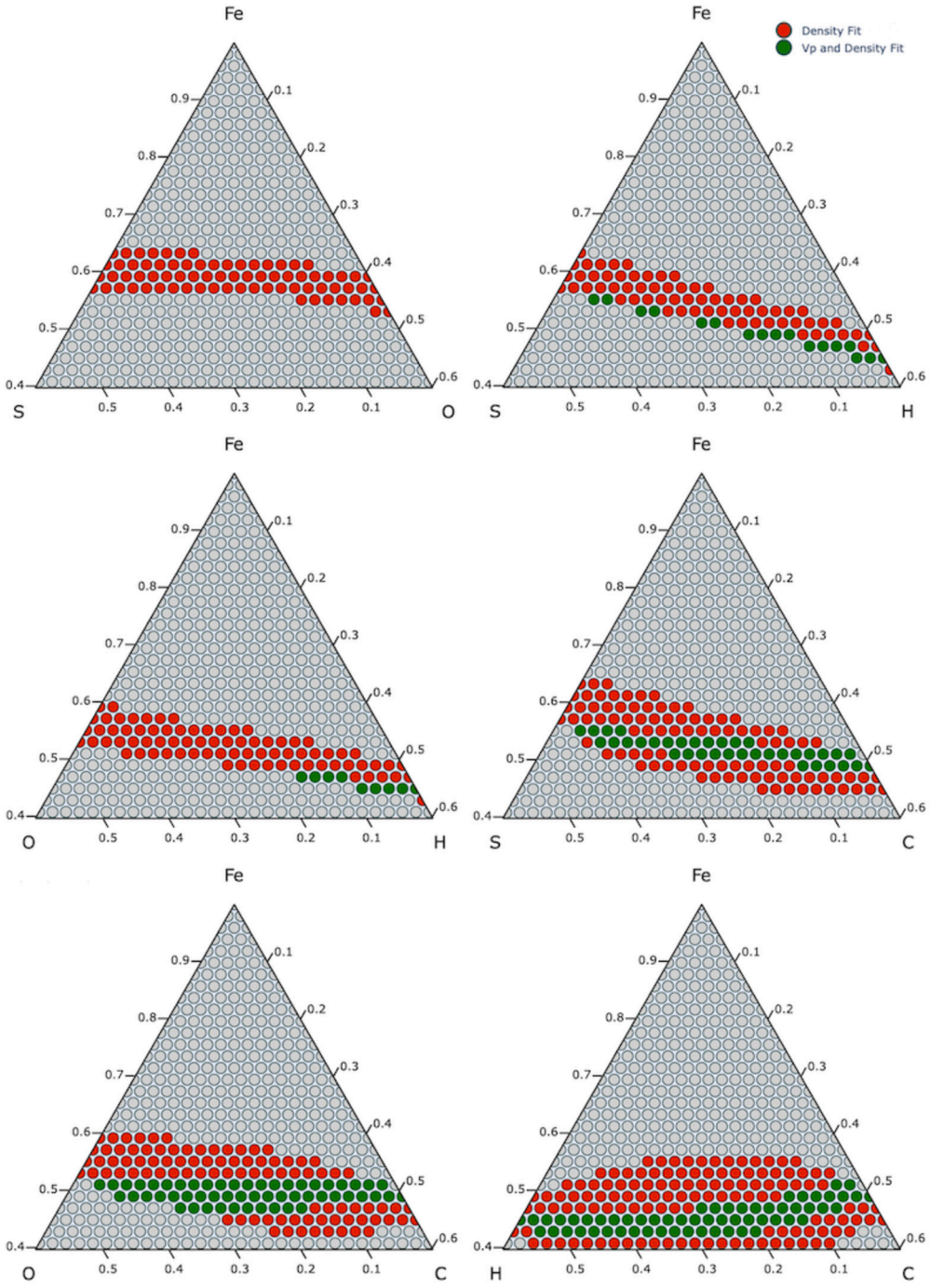

Fig. 9. This figure is similar to Figs. 7 and 8, but for the model proposed by Samuel et al. (2023). Red points show compositions which match just density and green points match both density and V_ϕ. The inversion assumes a starting temperature of the Martian CMB of 2850 K (see text).

4.3. Best fits

We now search for the 'best' Martian core composition across the full chemical range. We first consider solutions without any geochemical or partitioning constraints whatsoever. These results, therefore, encompass the fullest compositional space possible. We also consider possible CMB temperatures of 2050 K, 2450 K and 2850 K, which span the range suggested in the literature. The results are shown in the Supplementary Information. Not surprisingly, all three geophysical models for density, Vp and core size, can be matched by some sort of composition. Moreover, in agreement with previous studies, the core is very volatile rich, and contains between 45-55 mol% light elements (the exact wt% depends on the H content). Moreover, the best compositions all have high carbon contents of between 18 to 34 mol%. This large carbon content seems to be required as it decreases density and yet increases compressional wave speed relative to pure iron under Martian core conditions.

Finally we limit our search for solutions which are constrained to strictly incorporate geochemical and cosmochemical constraints. These constraints are 1) to explicitly limit sulphur to less than 17 wt% (Steenstra and van Westrenen, 2018), 2) to incorporate the positive correlation between S and O using the equation provided from Gendre et al. (2022), and 3) the simultaneous negative correlation between S and C content using the equation provided from Tsuno et al. (2018). As such, hydrogen is the only completely independent parameter allowed to vary

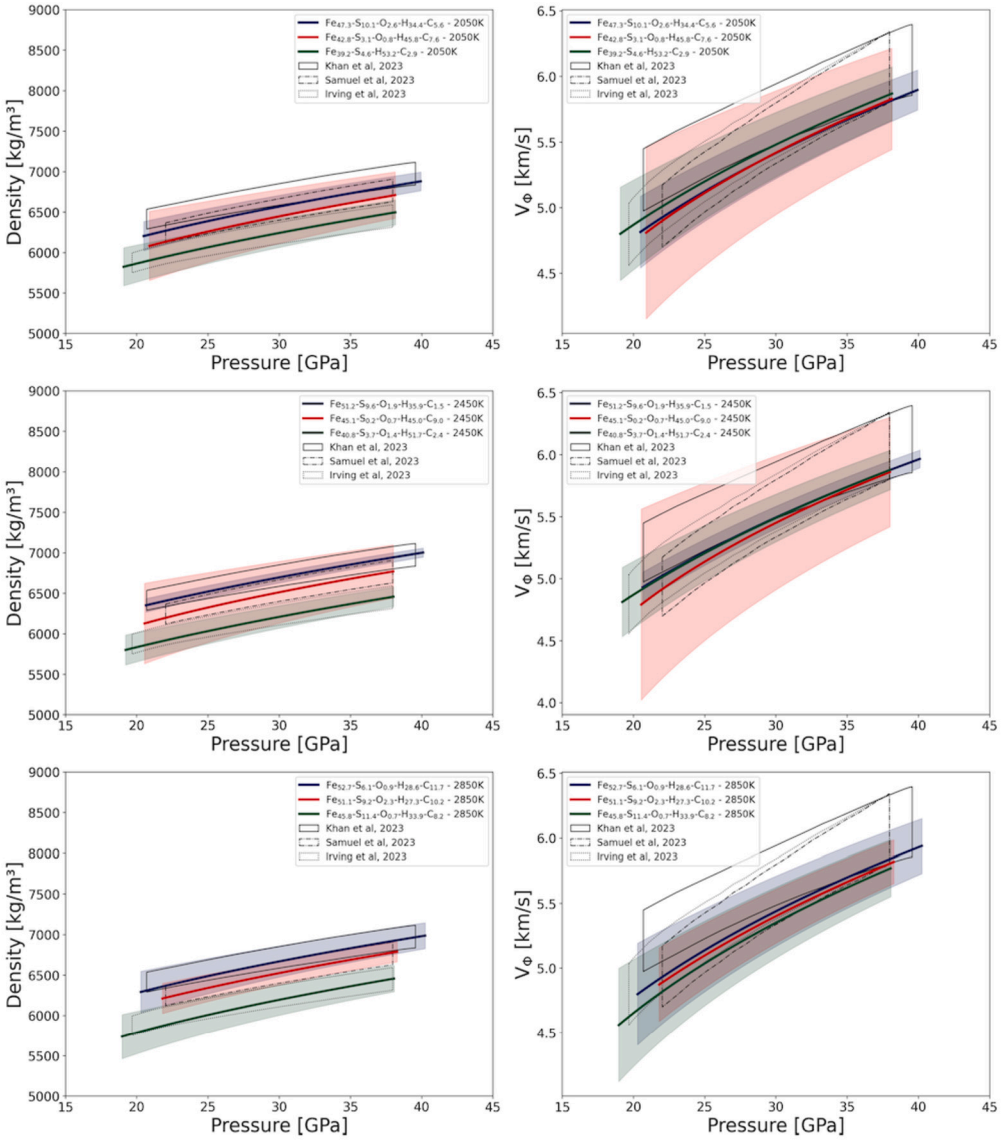

Fig. 10. Shows the density and compressional wave speeds of our best fit composition for the three geophysical models for the Martian core, with results constrained by geochemical considerations (see text). Results without geochemical considerations are shown in Fig. 9 of the Supplementary Information. The CMB temperatures used are 2050 K, 2450 K and 2850 K. All unconstrained searches contain between 45-55 mol% light element and require high concentrations of hydrogen and relatively low concentrations of oxygen.

freely in all cases. The results are shown in Fig. 10. Again, we find that the Martian core requires a high concentration of light elements (45-50 mol%), however, due to the geochemical limits on carbon, specifically its reduced affinity to partition into iron alloys with increasing sulphur concentration, the amount of carbon is significantly restricted. In addition oxygen concentrations are very low. Consequently, the Martian core in these models requires a higher concentration of hydrogen (>0.5 wt%) to match the density models.

5. Conclusions

In this work, we have modelled the Martian core composition through the development of a Gaussian process equation of state based on DFT simulations. Accurate treatment of the magnetic entropy via thermodynamic integration proved essential in matching our model with experimental observations of compressional wave speed and density. The development of the Gaussian process equation of state allows us to use thermodynamically consistent densities, velocities and compositionally dependent adiabats, enabling a more nuanced understanding of the Martian core's thermal and physical properties.

As with previous studies, we find there are a multitude of compositions which are able to fit the different density and velocity models proposed in the literature for the Martian core (Irving et al., 2023; Samuel et al., 2023; Khan et al., 2023). As with previous studies we require very high concentrations of light elements of 45 to 55 mol%.

Compositions that match the geophysical models with no geochemical or cosmochemical constraints are best matched with large amounts of C of between about 20 to 30 mol% (5 to 15 wt%). Although the liquidus temperatures of such alloys are still quite uncertain, these large concentrations may make an inner-core unlikely, although we accept that this requires more study.

Applying constraints from partitioning experiments and constraints on the maximum S content in the core very strongly shrinks the compositional space for the Martian core, and all compositions require a high concentration of hydrogen of > 27 mol% (>0.5 wt%) and very little oxygen.

Finally we note that while the temperature of the CMB could be an important constraint on the composition of the martian core, the range of temperatures tested here (between 1900 and 2850 K) are not so extreme as to excluded by any of the proposed geophysical models (density and V_ϕ) for the Martian core.

CRediT authorship contribution statement

Jac van Driel: Writing – review & editing, Writing – original draft, Visualization, Resources, Methodology, Formal analysis, Data curation, Conceptualization. **Lidunka Vočadlo:** Writing – review & editing, Writing – original draft, Supervision, Project administration, Investigation, Funding acquisition, Formal analysis, Conceptualization. **John Brodholt:** Writing – review & editing, Validation, Supervision, Resources, Project administration, Methodology, Investigation, Funding acquisition, Formal analysis, Conceptualization.

Declaration of competing interest

The authors declare that they have no known competing financial interests or personal relationships that could have appeared to influence the work reported in this paper.

Acknowledgements

We acknowledge funding from Science and Technology Facilities Council (STFC) (grant No. ST/T000163/1. This work used the ARCHER2 UK National Supercomputing Service (http://www.archer.ac.uk) and DiRAC High Performance Computing Facility (https://dirac.ac.uk).

Appendix A. Supplementary material

Supplementary material related to this article can be found online at https://doi.org/10.1016/j.epsl.2025.119540.

Data availability

Data will be made available on request.

References

Assael, M., Kakosimos, K., Banish, R., Brillo, J., Egry, I., Brooks, R., Quested, P., Mills, K., Nagashima, A., Sato, Y., Wakeham, W., 2006. Reference data for the density and viscosity of liquid aluminum and liquid iron. J. Phys. Chem. Ref. Data 35, 285–300. https://doi.org/10.1063/1.2149380.

Badro, J., Cote, A.S., Brodholt, J.P., 2014. A seismologically consistent compositional model of Earth's core. Proc. Natl. Acad. Sci. USA 111, 7542–7545. https://doi.org/10.1073/pnas.1316708111.

Blochl, P.E., 1994. Projector augmented-wave method. Phys. Rev. B 50, 17953–17979. https://doi.org/10.1103/PhysRevB.50.17953.

Brennan, M.C., Fischer, R.A., Irving, J.C.E., 2020. Core formation and geophysical properties of Mars. Earth Planet. Sci. Lett. 530. https://doi.org/10.1016/j.epsl.2019.115923.

Chen, J., Yu, T., Huang, S., Girard, J., Liu, X., 2014. Compressibility of liquid fes measured using x-ray radiograph imaging. Phys. Earth Planet. Inter. 228, 294–299. https://doi.org/10.1016/j.pepi.2013.12.012.

Edgington, A.L., Vocadlo, L., Stixrude, L., Wood, I.G., Dobson, D.P., Holmstrom, E., 2019. The top-down crystallisation of Mercury's core. Earth Planet. Sci. Lett. 528. https://doi.org/10.1016/j.epsl.2019.115838.

Flyvbjerg, H., Petersen, H.G., 1989. Error-estimates on averages of correlated data. J. Chem. Phys. 91, 461–466. https://doi.org/10.1063/1.457480.

Gardner, J.R., Pleiss, G., Bindel, D., Weinberger, K.Q., Wilson, A.G., 2018a. Gpytorch: blackbox matrix-matrix Gaussian process inference with gpu acceleration. In: Advances in Neural Information Processing Systems.

Gardner, J.R., Pleiss, G., Bindel, D., Weinberger, K.Q., Wilson, A.G., 2018b. Gpytorch: blackbox matrix-matrix Gaussian process inference with GPU acceleration. CoRR. arXiv:1809.11165.

Gendre, H., Badro, J., Wehr, N., Borensztajn, S., 2022. Martian core composition from experimental high-pressure metal-silicate phase equilibria. Geochem. Perspect. Lett. 21, 42–46. https://doi.org/10.7185/geochemlet.2216.

Holmstrom, E., Stixrude, L., 2015. Spin crossover in ferropericlase from first-principles molecular dynamics. Phys. Rev. Lett. 114. https://doi.org/10.1103/PhysRevLett.114.117202.

Huang, D., Li, Y., Khan, A., Sossi, P.A., Giardini, D., Murakami, M., 2023. Thermoelastic properties of liquid fe-rich alloys under martian core conditions. Geophys. Res. Lett. https://doi.org/10.1029/2022gl102271.

Irving, J.C.E., Lekić, V., Duran, C., Drilleau, M., Kim, D., Rivoldini, A., Khan, A., Samuel, H., Antonangeli, D., Banerdt, W.B., Beghein, C., Bozdağ, E., Ceylan, S., Charalambous, C., Clinton, J., Davis, P., Garcia, R., Giardini, N.D., Horleston, A.C., Huang, Q., Hurst, K.J., Kawamura, T., King, S.D., Knapmeyer, M., Li, J., Lognonné, P., Maguire, R., Panning, M.P., Plesa, A.C., Schimmel, M., Schmerr, N.C., Stähler, S.C., Stutzmann, E., Xu, Z., 2023. First observations of core-transiting seismic phases on Mars. https://doi.org/10.1073/pnas.2217090120.

Kawaguchi, S.I., Nakajima, Y., Hirose, K., Komabayashi, T., Ozawa, H., Tateno, S., Kuwayama, Y., Tsutsui, S., Baron, A.Q.R., 2017. Sound velocity of liquid fe-ni-s at high pressure. J. Geophys. Res., Solid Earth 122, 3624–3634. https://doi.org/10.1002/2016JB013609.

Kawaguchi, S.I., Morard, G., Kuwayama, Y., Hirose, K., Hirao, N., Ohishi, Y., 2022. Density determination of liquid iron-nickel-sulfur at high pressure. Am. Mineral. 107, 1254–1261. https://doi.org/10.2138/am-2021-7924.

Khan, A., Sossi, P.A., Liebske, C., Rivoldini, A., Giardini, D., 2022. Geophysical and cosmochemical evidence for a volatile-rich Mars. Earth Planet. Sci. Lett. 578. https://doi.org/10.1016/j.epsl.2021.117330.

Khan, A., Huang, D., Duran, C., Sossi, P., Giardini, D., Murakami, M., 2023. Evidence for a martian d″-like layer. https://doi.org/10.21203/rs.3.rs-2325906/v1.

Kresse, G., Furthmuller, J., 1996a. Efficiency of ab-initio total energy calculations for metals and semiconductors using a plane-wave basis set. Comput. Mater. Sci. 6, 15–50. https://doi.org/10.1016/0927-0256(96)00008-0.

Kresse, G., Furthmuller, J., 1996b. Efficient iterative schemes for ab initio total-energy calculations using a plane-wave basis set. Phys. Rev. B 54, 11169–11186. https://doi.org/10.1103/PhysRevB.54.11169.

Kresse, G., Hafner, J., 1993. Ab initio molecular-dynamics for liquid-metals. Phys. Rev. B 47, 558–561. https://doi.org/10.1103/PhysRevB.47.558.

Kresse, G., Hafner, J., 1994. Ab-initio molecular-dynamics simulation of the liquid-metal amorphous-semiconductor transition in germanium. Phys. Rev. B 49, 14251–14269. https://doi.org/10.1103/PhysRevB.49.14251.

Kresse, G., Joubert, D., 1999. From ultrasoft pseudopotentials to the projector augmented-wave method. Phys. Rev. B 59, 1758–1775. https://doi.org/10.1103/PhysRevB.59.1758.

Kuwayama, Y., Morard, G., Nakajima, Y., Hirose, K., Baron, A.Q.R., Kawaguchi, S.I., Tsuchiya, T., Ishikawa, D., Hirao, N., Ohishi, Y., 2020. Equation of state of liquid iron under extreme conditions. Phys. Rev. Lett. 124. https://doi.org/10.1103/PhysRevLett.124.165701.

Le Maistre, S., Rivoldini, A., Caldiero, A., Yseboodt, M., Baland, R.M., Beuthe, M., Van Hoolst, T., Dehant, V., Folkner, W.M., Buccino, D., Kahan, D., Marty, J.C., Antonangeli, D., Badro, J., Drilleau, M., Konopliv, A., Péters, M.J., Plesa, A.C., Samuel, H., Tosi, N., Wieczorek, M., Lognonné, P., Panning, M., Smrekar, S., Banerdt, W.B., 2023. Spin state and deep interior structure of Mars from insight radio tracking. Nature 619, 733–737. https://doi.org/10.1038/s41586-023-06150-0.

Li, Q., Xian, J.W., Zhang, Y., Sun, T., Vočadlo, L., 2022. Thermal properties of liquid iron at conditions of planetary cores. J. Geophys. Res. Planets 127, e2021JE007015. https://doi.org/10.1029/2021JE007015.

Morard, G., Siebert, J., Andrault, D., Guignot, N., Garbarino, G., Guyot, F., Antonangeli, D., 2013. The Earth's core composition from high pressure density measurements of liquid iron alloys. Earth Planet. Sci. Lett. 373, 169–178. https://doi.org/10.1016/j.epsl.2013.04.040.

Morard, G., Bouchet, J., Rivoldini, A., Antonangeli, D., Roberge, M., Boulard, E., Denoeud, A., Mezouar, M., 2018. Liquid properties in the fe-fes system under moderate pressure: tool box to model small planetary cores. Am. Mineral. 103, 1770–1779. https://doi.org/10.2138/am-2018-6405.

Nakajima, Y., Imada, S., Hirose, K., Komabayashi, T., Ozawa, H., Tateno, S., Tsutsui, S., Kuwayama, Y., Baron, A.Q.R., 2015. Carbon-depleted outer core revealed by sound velocity measurements of liquid iron-carbon alloy. Nat. Commun. 6. https://doi.org/10.1038/ncomms9942.

Nishida, K., Suzuki, A., Terasaki, H., Shibazaki, Y., Higo, Y., Kuwabara, S., Shimoyama, Y., Sakurai, M., Ushioda, M., Takahashi, E., Kikegawa, T., Wakabayashi, D., Funamori, N., 2016. Towards a consensus on the pressure and composition dependence of sound velocity in the liquid fe–s system. Phys. Earth Planet. Inter. 257. https://doi.org/10.1016/j.pepi.2016.06.009.

Nishida, K., Shibazaki, Y., Terasaki, H., Higo, Y., Suzuki, A., Funamori, N., Hirose, K., 2020. Effect of sulfur on sound velocity of liquid iron under martian core conditions. Nat. Commun. 11. https://doi.org/10.1038/s41467-020-15755-2.

Perdew, J.P., Burke, K., Ernzerhof, M., 1997. Generalized gradient approximation made simple (vol 77, pg 3865, 1996). Phys. Rev. Lett. 78, 1396. https://doi.org/10.1103/PhysRevLett.78.1396.

Pickard, C.J., Needs, R.J., 2011. Ab initio random structure searching. J. Phys. Condens. Matter 23, 053201. https://doi.org/10.1088/0953-8984/23/5/053201.

Rasmussen, C.E., Williams, C.K.I., 2006. Gaussian Processes for Machine Learning. Adaptive Computation and Machine Learning. MIT Press.

Samuel, H., Ballmer, M.D., Padovan, S., Tosi, N., Rivoldini, A., Plesa, A.C., 2021. The thermo-chemical evolution of Mars with a strongly stratified mantle. J. Geophys. Res. Planets 126. https://doi.org/10.1029/2020JE006613.

Samuel, H., Drilleau, M., Rivoldini, A., Xu, Z., Huang, Q., Garcia, R., Lekić, V., Irving, J., Badro, J., Lognonné, P., Connolly, J., Kawamura, T., Gudkova, T., Banerdt, W.,

2023. Geophysical evidence for an enriched molten silicate layer above Mars's core. Nature 622, 712–717. https://doi.org/10.1038/s41586-023-06601-8.

Shimoyama, Y., Terasaki, H., Ohtani, E., Urakawa, S., Takubo, Y., Nishida, K., Suzuki, A., Katayama, Y., 2013. Density of fe-3.5 wt% c liquid at high pressure and temperature and the effect of carbon on the density of the molten iron. Phys. Earth Planet. Inter. 224, 77–82. https://doi.org/10.1016/j.pepi.2013.08.003.

Shimoyama, Y., Terasaki, H., Urakawa, S., Takubo, Y., Kuwabara, S., Kishimoto, S., Watanuki, T., Machida, A., Katayama, Y., Kondo, T., 2016. Thermoelastic properties of liquid fe-c revealed by sound velocity and density measurements at high pressure. J. Geophys. Res., Solid Earth 121, 7984–7995. https://doi.org/10.1002/2016JB012968.

Stahler, S.C., Khan, A., Banerdt, W.B., Lognonne, P., Giardini, D., Ceylan, S., Drilleau, M., Duran, A.C., Garcia, R.F., Huang, Q.C., Kim, D., Lekic, V., Samuel, H., Schimmel, M., Schmerr, N., Sollberger, D., Stutzmann, E., Xu, Z.B., Antonangeli, D., Charalambous, C., Davis, P.M., Irving, J.C.E., Kawamura, T., Knapmeyer, M., Maguire, R., Marusiak, A.G., Panning, M.P., Perrin, C., Plesa, A.C., Rivoldini, A., Schmelzbach, C., Zenhausern, G., Beucler, E., Clinton, J., Dahmen, N., van Driel, M., Gudkova, T., Horleston, A., Pike, W.T., Plasman, M., Smrekar, S.E., 2021. Seismic detection of the martian core. Science 373, 443–448. https://doi.org/10.1126/science.abi7730.

Steenstra, E.S., van Westrenen, W., 2018. A synthesis of geochemical constraints on the inventory of light elements in the core of Mars. Icarus 315, 69–78. https://doi.org/10.1016/j.icarus.2018.06.023.

Terasaki, H., Nishida, K., Shibazaki, Y., Sakamaki, T., Suzuki, A., Ohtani, E., Kikegawa, T., 2010. Density measurement of fe3c liquid using x-ray absorption image up to 10 gpa and effect of light elements on compressibility of liquid iron. J. Geophys. Res., Solid Earth 115. https://doi.org/10.1029/2009JB006905.

Terasaki, H., Rivoldini, A., Shimoyama, Y., Nishida, K., Urakawa, S., Maki, M., Kurokawa, F., Takubo, Y., Shibazaki, Y., Sakamaki, T., Machida, A., Higo, Y., Uesugi, K., Takeuchi, A., Watanuki, T., Kondo, T., 2019. Pressure and composition effects on sound velocity and density of core-forming liquids: implication to core compositions of terrestrial planets. J. Geophys. Res. Planets 124, 2272–2293. https://doi.org/10.1029/2019JE005936.

Tsuno, K., Grewal, D.S., Dasgupta, R., 2018. Core-mantle fractionation of carbon in Earth and Mars: the effects of sulfur. Geochim. Cosmochim. Acta 238, 477–495. https://doi.org/10.1016/j.gca.2018.07.010.

Umemoto, K., Hirose, K., 2020. Chemical compositions of the outer core examined by first principles calculations. Earth Planet. Sci. Lett. 531, 116009. https://doi.org/10.1016/j.epsl.2019.116009.

Waseda, Y., Suzuki, K., 1970. Atomic distribution and magnetic moment in liquid iron by neutron diffraction. Phys. Status Solidi 39, 669. https://doi.org/10.1002/pssb.19700390235.

Weber, M., Knoll, W., Steeb, S., 1978. Magnetic small-angle scattering from molten elements iron, cobalt, and nickel. J. Appl. Crystallogr. 11, 638–641. https://doi.org/10.1107/S0021889878014107.

Xu, F., Morard, G., Guignot, N., Rivoldini, A., Manthilake, G., Chantel, J., Xie, L., Yoneda, A., King, A., Boulard, E., Pandolfi, S., Ryerson, F., Antonangeli, D., 2021. Thermal expansion of liquid fe-s alloy at high pressure. Earth Planet. Sci. Lett. 563, 116884. https://doi.org/10.1016/j.epsl.2021.116884.

Zhao, B., Morard, G., Boulard, E., Boccato, S., Siersch, N.C., Rivoldini, A., Guignot, N., Henry, L., King, A., Zurkowski, C., Fei, Y., Antonangeli, D., 2023. Local structure and density of liquid fe-c-s alloys at moon's core conditions. J. Geophys. Res. Planets 128, e2022JE007577. https://doi.org/10.1029/2022JE007577.